SUPPLEMENTARY FIGURES AND TABLES

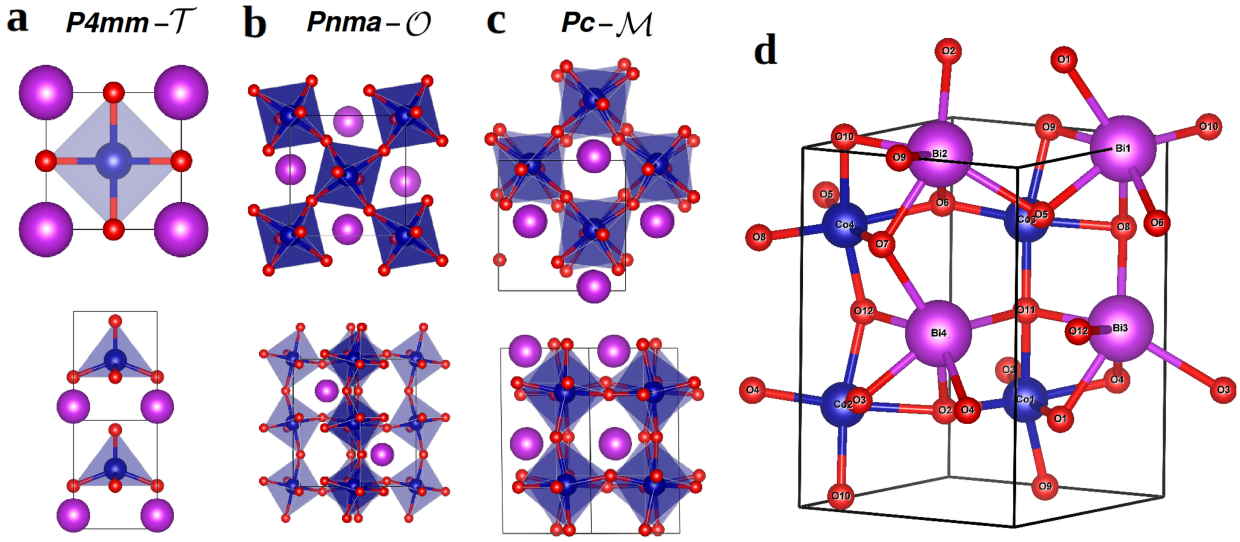

Supplementary Figure 1: Ball-stick representation of the competing phases in bulk stoichiometric $BiCoO_3$. **a** The ground-state super-tetragonal phase $\mathcal{T}$, and the metastable **b** orthorhombic $\mathcal{O}$ and **c** monoclinic $\mathcal{M}$ phases. **d** Atomic labelling employed in this work for the usual 20-atoms simulation cell.

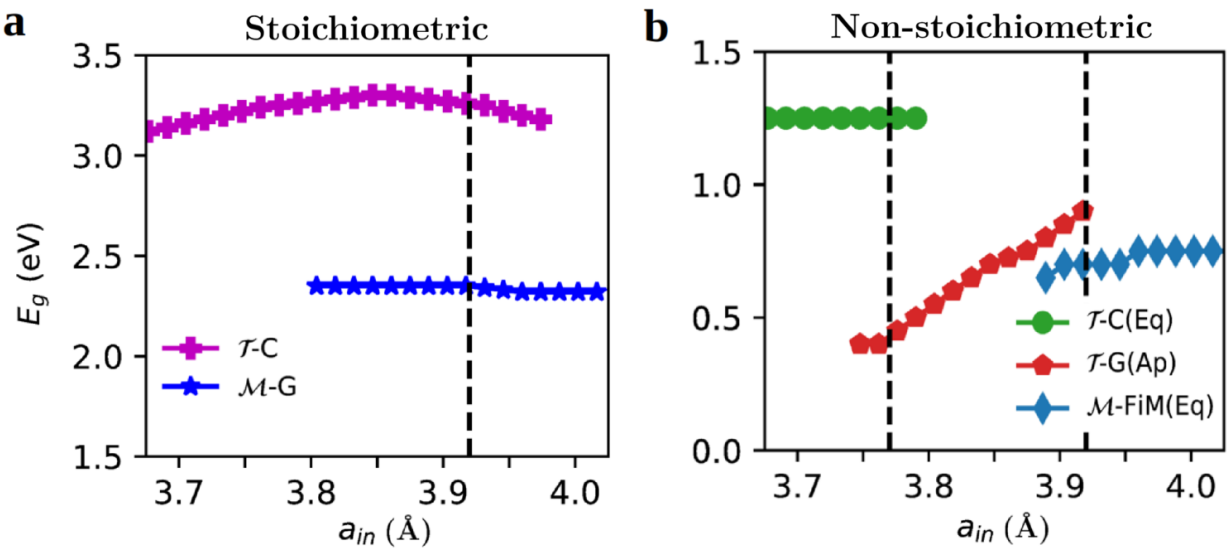

Supplementary Figure 2: Energy band gap, E_g, estimated in epitaxially grown $BiCoO_3$ thin films. **a** Stoichiometric and **b** non-stoichiometric cases of relevance. Results are obtained with the range-separated hybrid density functional theory functional HSE06 [1] on the equilibrium geometries determined with the PBE exchange-correlation potential ($U = 6$ eV) [2]. Dashed vertical lines mark the occurrence of strain-induced phase transitions.

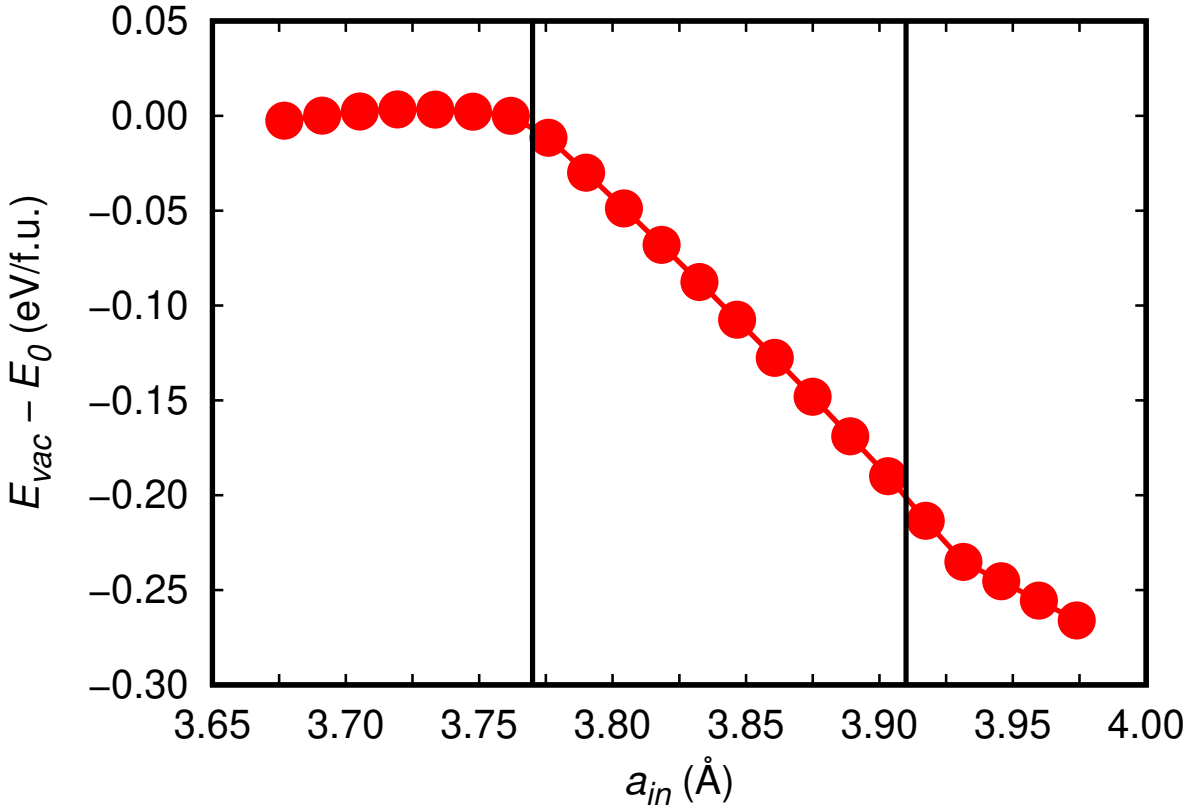

Supplementary Figure 3: Formation energy of oxygen vacancy in $BiCoO_3$ thin films (considering the most stable phases) expressed as a function of in-plane lattice parameter. A general energy shift, E_0, has been considered so that the oxygen vacancy formation energy corresponding to the bulk equilibrium stoichiometric system ($a_{in} = 3.76$ Å) is equal to zero. The solid vertical lines represent strain-induced phase transformations occurring in the off-stoichiometric systems. Results have been obtained with the PBE exchange-correlation potential ($U = 6$ eV) [2].

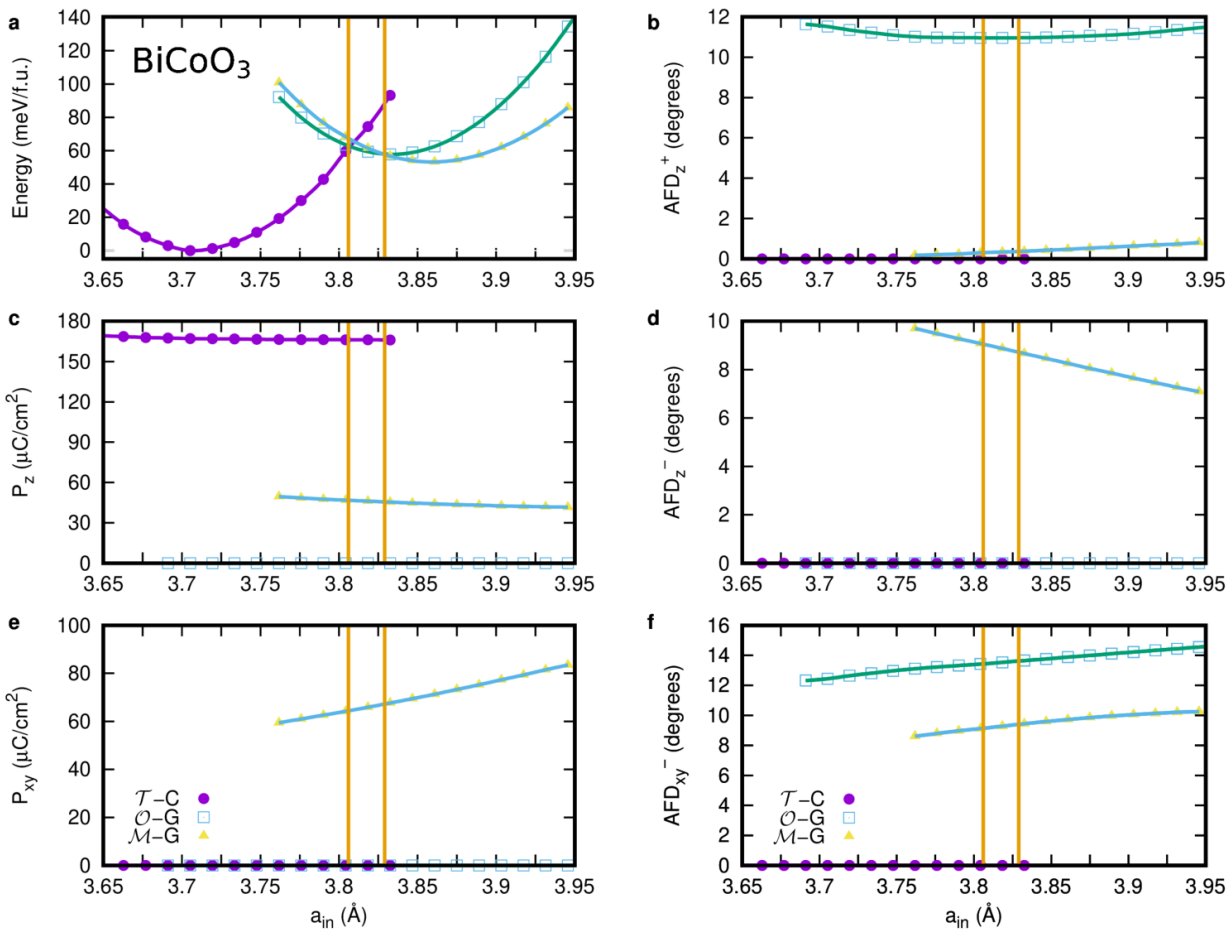

Supplementary Figure 4: Energy, structural, and ferroelectric properties of competing polymorphs in stoichiometric $BiCoO_3$ thin films calculated with the PBEsol density functional theory functional ($U = 6$ eV) [3]. **a** Zero-temperature total energy, **b** in-phase oxygen octahedral rotation angles along the (100) direction, **c** electric polarization along the (100) direction, **d** anti-phase oxygen octahedral rotation angles along the (100) direction, **e** electric polarization along the (011) direction, **f** anti-phase oxygen octahedral rotation angles along the (011) direction. The vertical lines indicate strain-induced $\mathcal{T} \rightarrow \mathcal{O}$ and $\mathcal{O} \rightarrow \mathcal{M}$ phase transitions at low temperatures. Analogous results obtained with the PBE exchange-correlation functional [2] are reported in the main text and work [4].

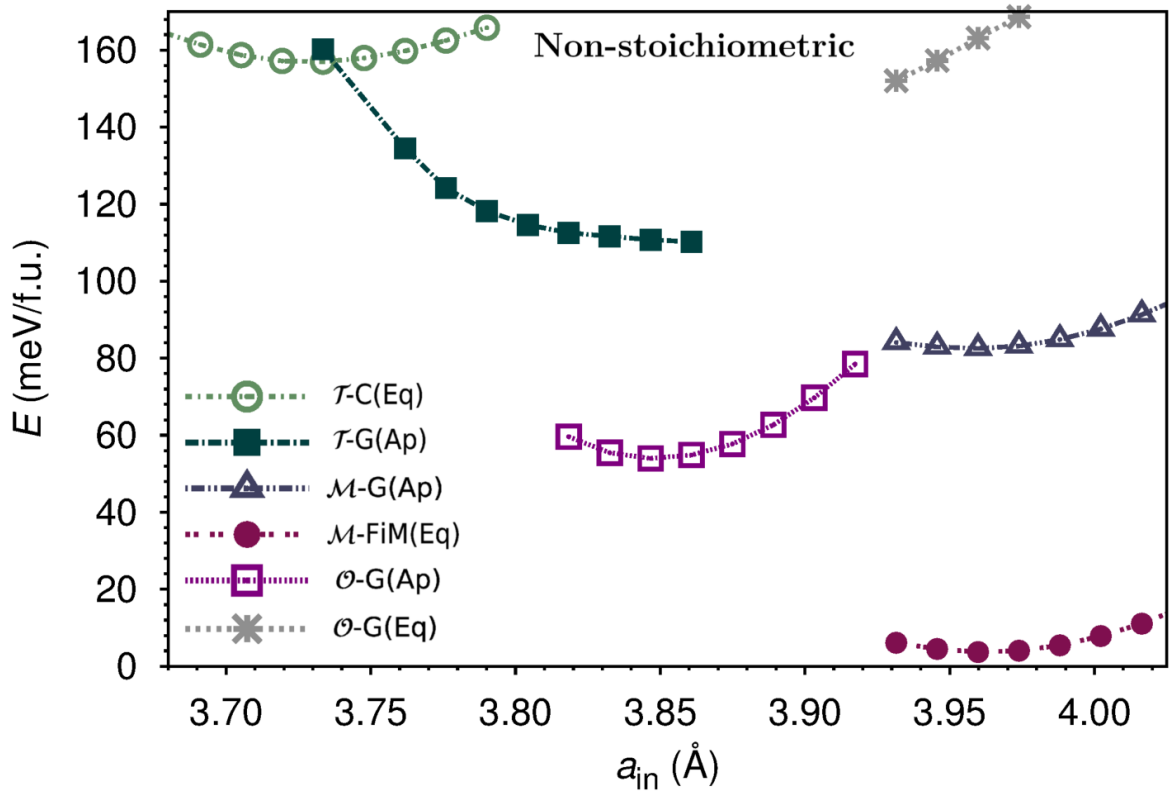

Supplementary Figure 5: Effects of neutral V_O's on phase competition in $BiCoO_3$ thin films as calculated with the PBEsol density functional theory functional ($U = 6$ eV) [3]. Oxygen vacancy positions leading to lowest energy, either apical "Ap" or equatorial "Eq", is indicated within parentheses. "G" stands for G-type antiferromagnetism, "C" for C-type antiferromagnetism, and "FiM" for ferrimagnetism.

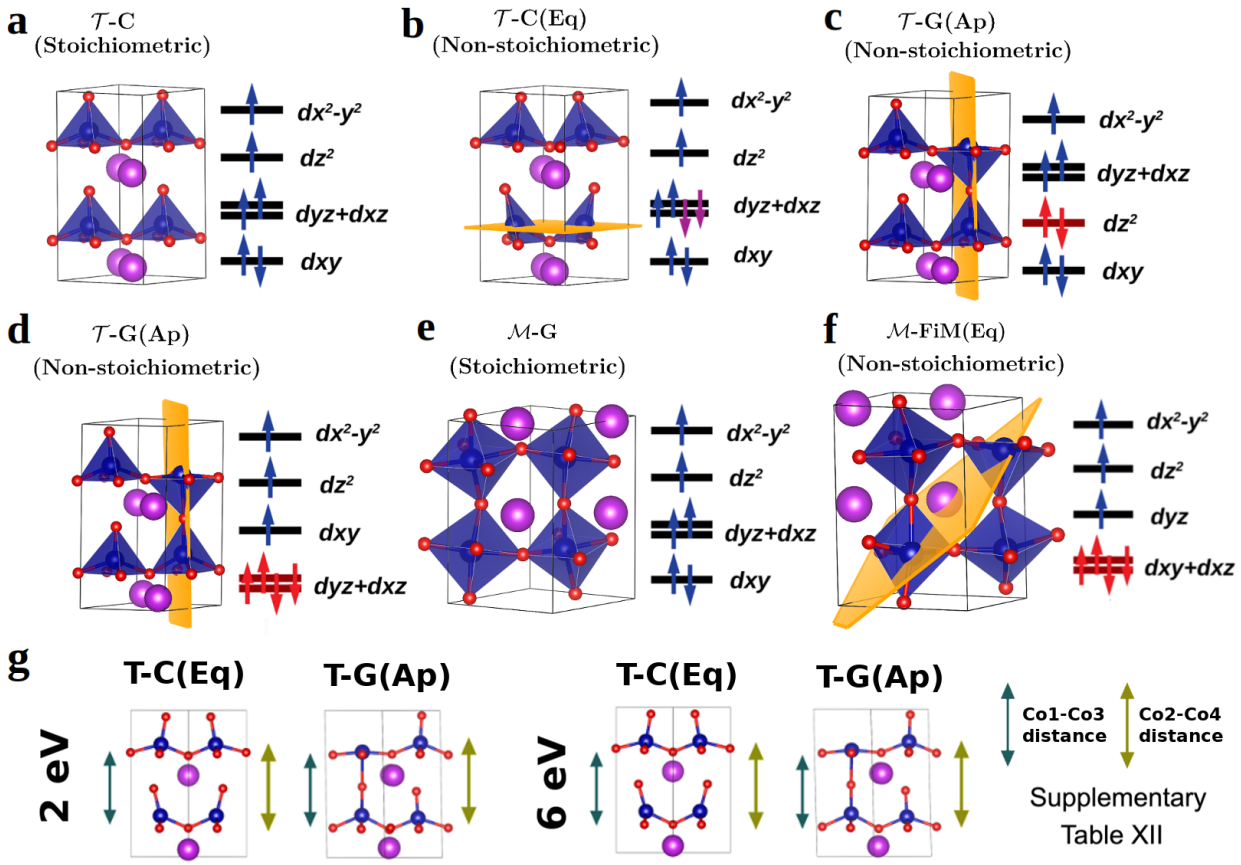

Supplementary Figure 6: Transition metal electronic-orbital occupation in $BiCoO_3$ thin films as calculated with the PBE exchange-correlation potential ($U = 2$ eV) [2]. The orange planes indicate the two Co ions that are reduced as a consequence of creating a neutral oxygen vacancy. The purple arrows in **b** indicate electronic delocalization among two different d orbitals. The red arrows in **c**, **d**, and **f** indicate differences with respect to the stoichiometric cases **a** and **e**. **g** Geometry variations resulting from the choice of U value (see Supplementary Table XII for the corresponding numerical values).

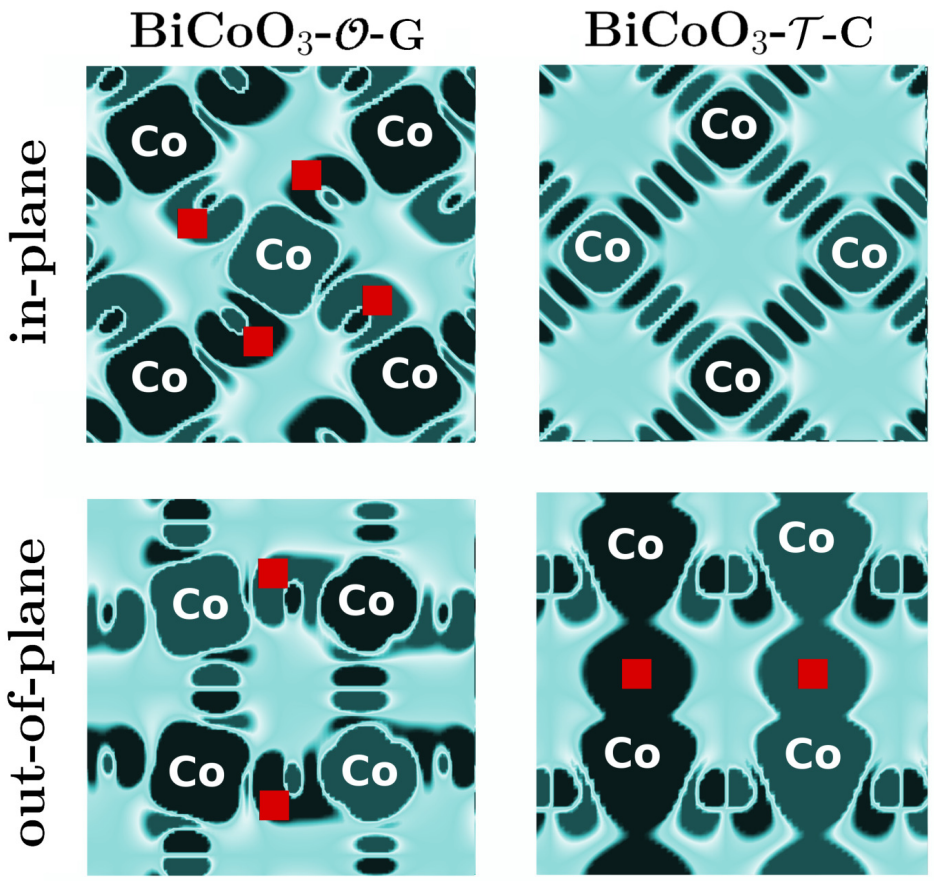

Supplementary Figure 7: Spin-up (dark green) and spin-down (light green) electronic charge densities calculated in stoichiometric $\mathcal{T}$ and $\mathcal{O}$ $BiCoO_3$ thin films considering two perpendicular planes. Highly magnetized oxygen atoms are indicated with red squares. Results are obtained with PBE exchange-correlation potential ($U = 6$ eV) [2].

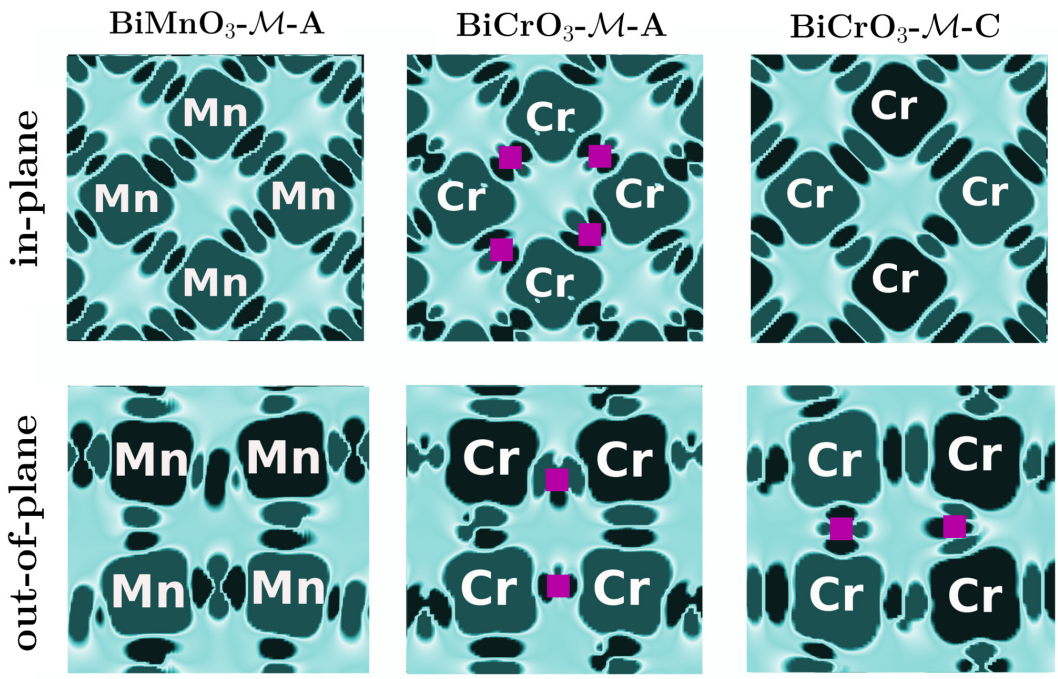

Supplementary Figure 8: Spin-up (dark green) and spin-down (light green) electronic charge densities calculated in stoichiometric $\mathcal{M}$ $BiMnO_3$ and $BiCrO_3$ thin films considering two perpendicular planes. Magnetized oxygen atoms are indicated with purple squares. Results are obtained with PBE exchange-correlation potential ($U = 4$ eV) [2].

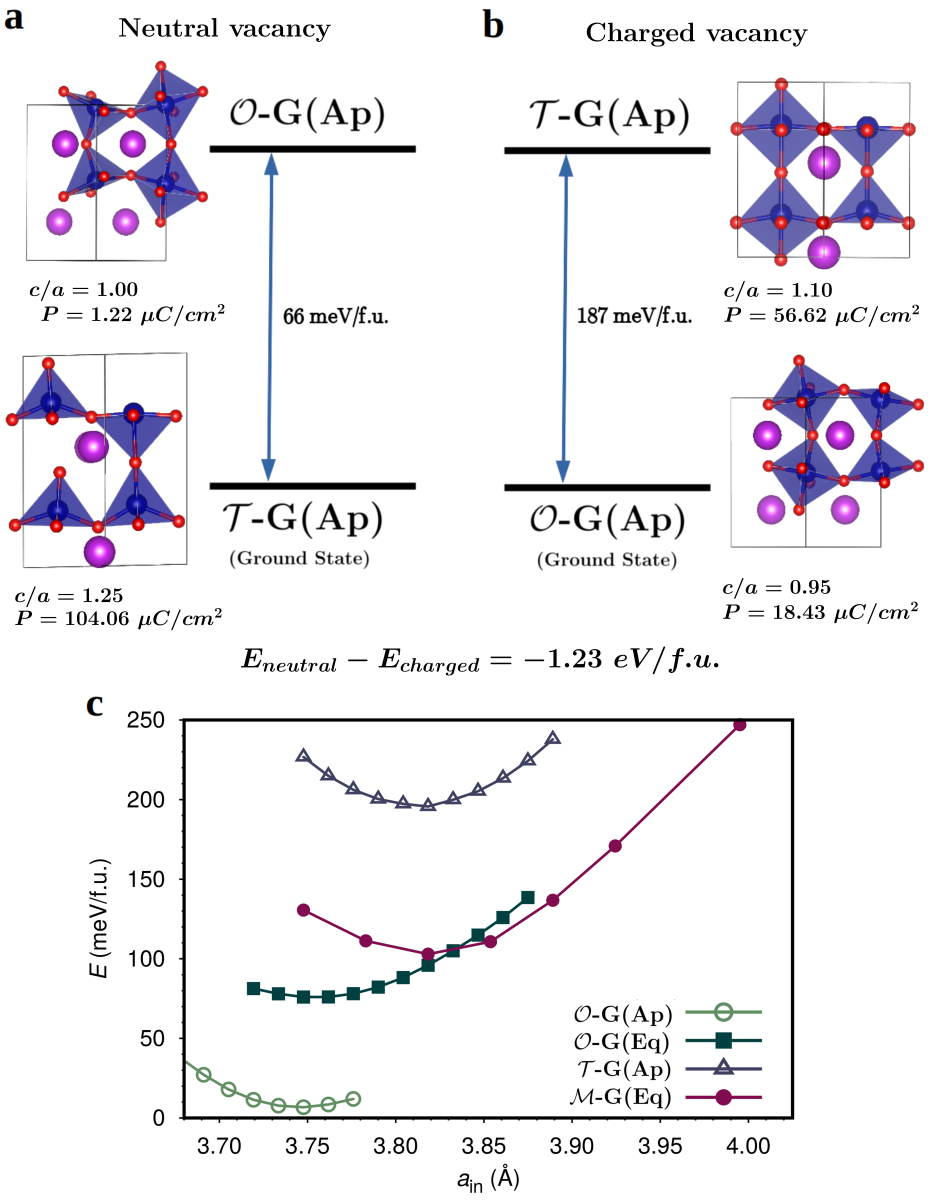

Supplementary Figure 9: Neutral versus charged ($q = +2\ e$) oxygen vacancies in $BiCoO_3$ thin films. **a** Energy difference between the ground state and lowest-energy metastable phase at $a_{in} = 3.78$ Å when considering neutral oxygen vacancies. **b** Energy difference between the ground state and lowest-energy metastable phase at $a_{in} = 3.78$ Å when considering charged oxygen vacancies. At zero temperature, the formation of neutral vacancies is energetically more favourable than charged vacancies ($\Delta E_{def} \equiv E_{def}[V_O^0] - E_{def}[V_O^{+2}] \sim -1$ eV/f.u.). **c** Effects of charged V_O's on the phase competition of $BiCoO_3$ thin films. Results are obtained with the PBE functional ($U = 6$ eV) [2].

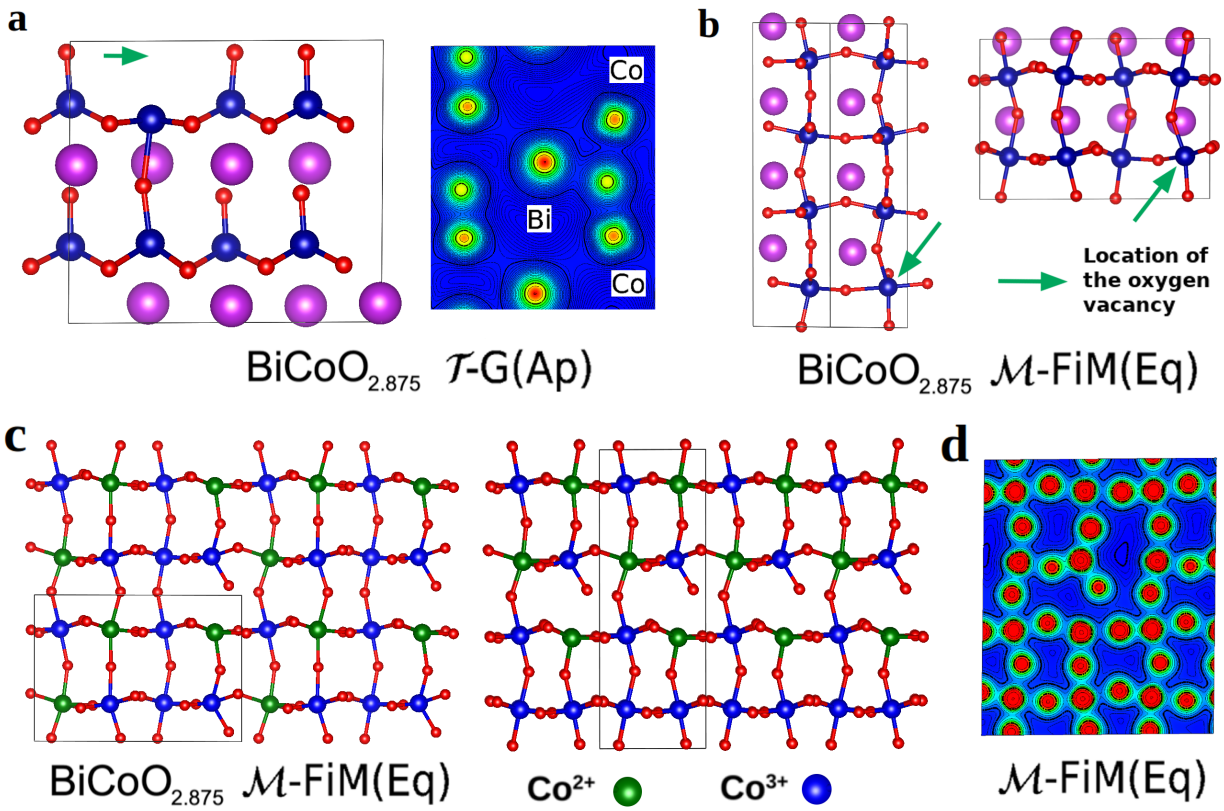

Supplementary Figure 10: 40-atoms simulations cells employed for estimating size effects in our calculations for $BiCoO_{3-x}$ thin films. **a** $\mathcal{T}$-G(Ap) and **b** $\mathcal{M}$-FiM(Eq). Green arrows indicate the location of the oxygen vacancies. **c** Lowest-energy distribution of Co^{2+} and Co^{3+} ions in $BiCoO_{2.875}$ thin films, which results in a ferrimagnetic state. Charge density surface plot calculated for $\mathcal{M}$-FiM(Eq) $BiCoO_{2.875}$ thin films. Results are analogous to those reported for $\mathcal{M}$-FiM(Eq) $BiCoO_{2.75}$ thin films in Fig.4e of the main text. Results are obtained with the PBE functional ($U = 6$ eV) [2].

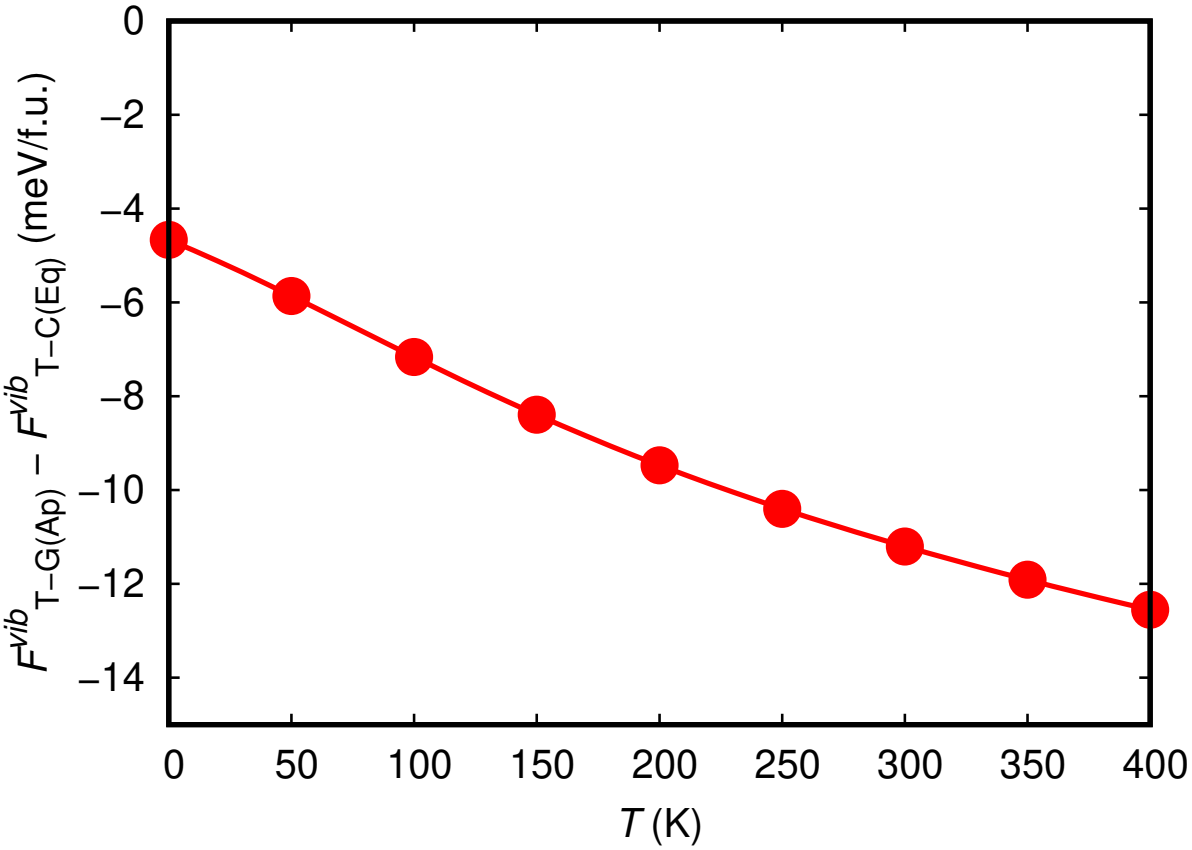

Supplementary Figure 11: Vibrational Helmholtz free energy difference calculated for non-stoichiometric $\mathcal{T}$ phases containing oxygen vacancies at apical and equatorial positions for the in-plane lattice parameter $a_{in} = 3.78$ Å . The vibrational Helmholtz free energies have been calculated considering only Γ-point phonon frequencies. At the selected a_{in}, the $\mathcal{T}$-G(Ap) is vibrationally softer than $\mathcal{T}$-C(Eq) thus entropy contributions favour the stabilization of the former phase at finite temperatures. Results are obtained with the PBE functional ($U = 6$ eV) [2].

Supplementary Table I: Data obtained with the PBE functional ($U = 6$ eV) [2].

$BiCoO_3$ $\mathcal{T}$-C [Space group $P4mm$] Bulk					
a (Å)	b (Å)	c (Å)	α (°)	β (°)	γ (°)
3.7208	3.7208	4.6410	90.0000	90.0000	90.0000

Atom	Wyckoff position	x	y	z
Co	**1b** (z = -0.45439)			
1		0.50000	0.50000	0.54561
Bi	**1a** (z = 0.11113)			
2		0.00000	0.00000	0.11113
O1	**1b** (z = -0.07636)			
3		0.50000	0.50000	0.92364
O2	**2c** (z = 0.39874)			
4		0.50000	0.00000	0.39874
5		0.00000	0.50000	0.39874

Supplementary Table II: Data obtained with the PBE functional ($U = 6$ eV) [2].

$BiCoO_3$ $\mathcal{O}$-G [Space group $Pnma$] Bulk					
a (Å)	b (Å)	c (Å)	α (°)	β (°)	γ (°)
5.5764	7.9408	5.4426	90.0000	90.0000	90.0000

Atom	Wyckoff position	x	y	z
Co	**4a** (x = 0.00000, z = 0.00000)			
1		0.00000	0.00000	0.00000
2		0.00000	0.50000	0.00000
3		0.50000	0.50000	0.50000
4		0.50000	0.00000	0.50000
Bi	**4c** (x = 0.45051, z = -0.00335)			
5		0.45051	0.25000	0.99665
6		0.95051	0.25000	0.50335
7		0.04949	0.75000	0.49665
8		0.54949	0.75000	0.00335
O1	**4c** (x = -0.47048, z = 0.40844)			
9		0.52952	0.25000	0.40844
10		0.02952	0.25000	0.09156
11		0.97048	0.75000	0.90844
12		0.47048	0.75000	0.59156
O2	**8d** (x = -0.28986, y = 0.45893)			
13		0.71014	0.45893	0.81378
14		0.78986	0.54107	0.31378
15		0.21014	0.04107	0.68622
16		0.28986	0.95893	0.18622
17		0.28986	0.54107	0.18622
18		0.21014	0.45893	0.68622
19		0.78986	0.95893	0.31378
20		0.71014	0.04107	0.81378

Supplementary Table III: Data obtained with the PBE functional ($U = 6$ eV) [2].

$BiCoO_3$ $\mathcal{M}$-G [Space group Pc] Bulk					
a (Å)	b (Å)	c (Å)	α (°)	β (°)	γ (°)
8.0871	5.5277	5.5840	90.0000	90.6971	90.0000

Atom	Wyckoff position	x	y	z
Co1	**2a** (x = 0.26342, y = -0.24839, z = 0.47033)			
1		0.26342	0.75161	0.47033
2		0.26342	0.24839	0.97033
Co2	**2a** (x = -0.23602, y = -0.25063, z = 0.47053)			
3		0.76398	0.74937	0.47053
4		0.76398	0.25063	0.97053
Bi1	**2c** (x = -0.01333, y = -0.24519, z = 0.02692)			
5		0.98667	0.75481	0.02692
6		0.98667	0.24519	0.52692
Bi2	**2c** (x = 0.48634, y = -0.25392, z = 0.02933)			
7		0.48634	0.74608	0.02933
8		0.48634	0.25392	0.52933
O1	**2c** (x = 0.25015, y = -0.46435, z = 0.15163)			
9		0.25015	0.53565	0.15163
10		0.25015	0.46435	0.65163
O2	**2c** (x = 0.31191, y = -0.01115, z = -0.26351)			
11		0.31191	0.98885	0.73649
12		0.31191	0.01115	0.23649
O3	**2d** (x = -0.18592, y = 0.46566, z = 0.22128)			
13		0.81408	0.46566	0.22128
14		0.81408	0.53434	0.72128

Atom	Wyckoff position	x	y	z
O4	**2d** (x = -0.25017, y = 0.05720, z = -0.33516)			
15		0.74983	0.05720	0.66484
16		0.74983	0.94280	0.16484
O5	**2d** (x = 0.01994, y = -0.17821, z = 0.43177)			
17		0.01994	0.82179	0.43177
18		0.01994	0.17821	0.93177
O6	**2d** (x = -0.47924, y = -0.31722, z = 0.43472)			
19		0.52076	0.68278	0.43472
20		0.52076	0.31722	0.93472

Supplementary Table IV: Data obtained with the PBE functional ($U = 6$ eV) [2].

$BiCoO_{3-x}$ $\mathcal{T}$-C(Eq) [Space group $P1$]					
a (Å)	b (Å)	c (Å)	α (°)	β (°)	γ (°)
5.3400	5.3400	9.6050	90.0011	90.0024	90.0000

Atom	Wyckoff position	x	y	z
Co1	**1a** (x = 0.02675, y = -0.49404, z = 0.28295)	0.02675	0.50596	0.28295
Co2	**1a** (x = 0.49959, y = 0.03307, z = 0.28288)	0.49959	0.03307	0.28288
Co3	**1a** (x = 0.02733, y = -0.49462, z = -0.23422)	0.02733	0.50538	0.76578
Co4	**1a** (x = 0.49910, y = 0.03364, z = -0.23414)	0.49910	0.03364	0.76586
Bi1	**1a** (x = 0.04295, y = 0.04946, z = 0.04635)	0.04295	0.04946	0.04635
Bi2	**1a** (x = 0.48323, y = 0.48971, z = 0.04634)	0.48323	0.48971	0.04634
Bi3	**1a** (x = -0.01002, y = -0.00372, z = -0.44121)	0.98998	0.99628	0.55879
Bi4	**1a** (x = -0.46362, y = -0.45726, z = -0.44120)	0.53638	0.54274	0.55880
O1	**1a** (x = 0.07009, y = 0.46265, z = -0.04621)	0.07009	0.46265	0.95379
O2	**1a** (x = 0.45638, y = 0.07636, z = -0.04616)	0.45638	0.07636	0.95384
O3	**1a** (x = -0.23682, y = 0.26953, z = 0.19244)	0.76318	0.26953	0.19244
O4	**1a** (x = 0.26317, y = 0.26956, z = 0.19288)	0.26317	0.26956	0.19288
O5	**1a** (x = 0.26307, y = -0.23045, z = 0.19241)	0.26307	0.76955	0.19241
O6	**1a** (x = -0.03824, y = -0.42894, z = 0.47184)	0.96176	0.57106	0.47184
O7	**1a** (x = -0.43524, y = -0.03217, z = 0.47174)	0.56476	0.96783	0.47174
O8	**1a** (x = -0.23679, y = -0.23049, z = -0.28391)	0.76321	0.76951	0.71609
O9	**1a** (x = -0.23680, y = 0.26949, z = -0.29389)	0.76320	0.26949	0.70611
O10	**1a** (x = 0.26323, y = 0.26949, z = -0.30793)	0.26323	0.26949	0.69207
O11	**1a** (x = 0.26323, y = -0.23049, z = -0.29389)	0.26323	0.76951	0.70611

Supplementary Table V: Data obtained with the PBE functional ($U = 6$ eV) [2].

$BiCoO_{3-x}$ $\mathcal{T}$-G(Ap) [Space group $P1$]					
a (Å)	b (Å)	c (Å)	α (°)	β (°)	γ (°)
5.3400	5.3400	9.6953	90.7799	90.9864	90.0000

Atom	Wyckoff position	x	y	z
Co1	**1a** (x = -0.38044, y = 0.47505, z = 0.28886)	0.13951	0.47505	0.28886
Co2	**1a** (x = 0.15982, y = -0.03380, z = 0.26786)	0.61956	0.96620	0.26786
Co3	**1a** (x = -0.34473, y = 0.48772, z = -0.27887)	0.15982	0.48772	0.72113
Co4	**1a** (x = 0.10129, y = -0.00095, z = -0.22128)	0.65527	0.99905	0.77872
Bi1	**1a** (x = -0.37645, y = -0.03138, z = 0.06641)	0.10129	0.96862	0.06641
Bi2	**1a** (x = 0.16298, y = 0.45410, z = 0.06718)	0.62355	0.45410	0.06718
Bi3	**1a** (x = -0.32470, y = -0.02712, z = -0.43550)	0.16298	0.97288	0.56450
Bi4	**1a** (x = -0.32906, y = 0.49583, z = -0.43737)	0.67530	0.49583	0.56263
O1	**1a** (x = 0.37563, y = 0.01209, z = -0.03769)	0.67094	0.01209	0.96231
O2	**1a** (x = 0.37217, y = 0.22155, z = 0.19251)	0.37563	0.22155	0.19251
O3	**1a** (x = -0.12679, y = -0.28188, z = 0.18710)	0.37217	0.71812	0.18710
O4	**1a** (x = -0.12200, y = -0.27756, z = 0.19307)	0.87321	0.72244	0.19307
O5	**1a** (x = 0.09602, y = 0.22438, z = 0.20027)	0.87800	0.22438	0.20027
O6	**1a** (x = -0.38969, y = -0.47126, z = 0.48553)	0.09602	0.52874	0.48553
O7	**1a** (x = 0.41007, y = -0.03770, z = 0.44691)	0.61031	0.96230	0.44691
O8	**1a** (x = 0.41268, y = -0.23124, z = -0.29739)	0.41007	0.23124	0.70261
O9	**1a** (x = -0.10268, y = 0.24977, z = -0.29640)	0.41268	0.75023	0.70360
O10	**1a** (x = -0.10684, y = -0.24802, z = -0.29233)	0.89732	0.75198	0.70767
O11	**1a** (x = -0.10684, y = 0.23712, z = -0.29922)	0.89316	0.23712	0.70078

Supplementary Table VI: Data obtained with the PBE functional ($U = 6$ eV) [2].

$BiCoO_{3-x}$ $\mathcal{M}$-FiM(Eq) [Space group $P1$]					
a (Å)	b (Å)	c (Å)	α (°)	β (°)	γ (°)
5.6800	5.6800	8.0605	90.9091	90.5248	90.0000

Atom	Wyckoff position	x	y	z
Co1	**1a** (x = -0.26469, y = -0.45404, z = -0.25378)	0.73531	0.54596	0.74622
Co2	**1a** (x = 0.29228, y = 0.02108, z = -0.25912)	0.29228	0.02108	0.74088
Co3	**1a** (x = -0.25265, y = -0.47963, z = 0.23095)	0.74735	0.52037	0.23095
Co4	**1a** (x = 0.25250, y = 0.03284, z = 0.24560)	0.25250	0.03284	0.24560
Bi1	**1a** (x = -0.25670, y = -0.03124, z = 0.03177)	0.74330	0.96876	0.03177
Bi2	**1a** (x = 0.23470, y = 0.47075, z = 0.02011)	0.23470	0.47075	0.02011
Bi3	**1a** (x = -0.17804, y = -0.05890, z = -0.49556)	0.82196	0.94110	0.50444
Bi4	**1a** (x = 0.29291, y = 0.48425, z = -0.49730)	0.29291	0.48425	0.50270
O1	**1a** (x = -0.43600, y = -0.14113, z = -0.24617)	0.56400	0.85887	0.75383
O2	**1a** (x = 0.44029, y = 0.34851, z = -0.26017)	0.44029	0.34851	0.73983
O3	**1a** (x = 0.04372, y = -0.26995, z = -0.32528)	0.04372	0.73005	0.67472
O4	**1a** (x = 0.48076, y = -0.23341, z = 0.19086)	0.48076	0.76659	0.19086
O5	**1a** (x = -0.49527, y = 0.27266, z = 0.18975)	0.50473	0.27266	0.18975
O6	**1a** (x = 0.02836, y = 0.33621, z = 0.23587)	0.02836	0.33621	0.23587
O7	**1a** (x = -0.04469, y = -0.17021, z = 0.25788)	0.95531	0.82979	0.25788
O8	**1a** (x = -0.18001, y = -0.42648, z = -0.01524)	0.81999	0.57352	0.98476
O9	**1a** (x = 0.14422, y = 0.09240, z = -0.05976)	0.14422	0.09240	0.94024
O10	**1a** (x = -0.30758, y = -0.44138, z = 0.47771)	0.69242	0.55862	0.47771
O11	**1a** (x = 0.20851, y = 0.09684, z = -0.49032)	0.20851	0.09684	0.50968

Supplementary Table VII: Data obtained with the PBE functional ($U = 6$ eV) [2] in $\mathcal{M}$ $BiCoO_3$ thin films at $a_{in} = 4.01$ Å. The figures represent distances between pairs of Bi and O atoms as labelled in Supplementary Fig.1 and expressed in units of Å. In the $\mathcal{M}$-FiM(Eq) ($\mathcal{M}$-G(Ap)) phase, the Bi and O atoms surrounding the neutral oxygen vacancy in average move closer to (away from) each other as compared to the perfect stoichiometric system (see negative and positive signs in the column "Total").

Bi1	O1	O5	O6	O8	O9	O10	Total (Å)
$\mathcal{M}$-G	2.51	2.35	2.57	2.33	2.29	2.48	-
$\mathcal{M}$-FiM(Eq)	+0.01	-0.05	-0.05	-0.01	+0.03	+0.02	-0.05
$\mathcal{M}$-G(Ap)	$\mathbf{V_O}$	+0.12	+0.04	-0.07	-0.04	-0.16	-0.11
Bi2	O2	O5	O6	O7	O9	O10	Total (Å)
$\mathcal{M}$-G	2.51	2.57	2.35	2.33	2.48	2.29	-
$\mathcal{M}$-FiM(Eq)	+0.13	-0.01	-0.01	-0.08	-0.04	0.00	-0.01
$\mathcal{M}$-G(Ap)	-0.12	-0.09	-0.07	+0.04	+0.13	+0.05	-0.06
Bi3	O1	O3	O4	O8	O11	O12	Total (Å)
$\mathcal{M}$-G	2.38	2.63	2.28	2.43	2.28	2.54	-
$\mathcal{M}$-FiM(Eq)	+0.17	$\mathbf{V_O}$	-0.06	-0.21	+0.02	-0.18	-0.26
$\mathcal{M}$-G(Ap)	$\mathbf{V_O}$	-0.19	-0.05	-0.09	+0.06	-0.08	-0.19
Bi4	O2	O3	O4	O7	O11	O12	Total (Å)
$\mathcal{M}$-G	2.38	2.28	2.63	2.43	2.54	2.28	-
$\mathcal{M}$-FiM(Eq)	-0.15	$\mathbf{V_O}$	-0.21	+0.31	-0.23	-0.03	-0.31
$\mathcal{M}$-G(Ap)	-0.07	-0.08	+0.62	-0.03	0.00	-0.02	+0.42

Supplementary Table VIII: Data obtained with the PBE functional ($U = 4$ eV) [2].

$BiFeO_{3-x}$ $\mathcal{M}$-G(Ap) [Space group $P1$]					
a (Å)	b (Å)	c (Å)	α (°)	β (°)	γ (°)
5.6800	5.6800	8.1994	91.7596	90.5360	90.0000

Atom	Wyckoff position	x	y	z
Fe1	**1a** (x = -0.02232, y = -0.48609, z = 0.20370)	0.97768	0.51391	0.20370
Fe2	**1a** (x = -0.46408, y = 0.00494, z = 0.18904)	0.53592	0.00494	0.18904
Fe3	**1a** (x = 0.01617, y = 0.49967, z = -0.32177)	0.01617	0.49967	0.67823
Fe4	**1a** (x = -0.46521, y = 0.00713, z = -0.29614)	0.53479	0.00713	0.70386
Bi1	**1a** (x = 0.02661, y = -0.04699, z = -0.03612)	0.02661	0.95301	0.96388
Bi2	**1a** (x = 0.48703, y = 0.45585, z = -0.03581)	0.48703	0.45585	0.96419
Bi3	**1a** (x = 0.03958, y = -0.05048, z = 0.48552)	0.03958	0.94952	0.48552
Bi4	**1a** (x = -0.48917, y = 0.44811, z = 0.48111)	0.51083	0.44811	0.48111
O1	**1a** (x = -0.41569, y = 0.06418, z = -0.06037)	0.58431	0.06418	0.93963
O2	**1a** (x = -0.17662, y = -0.16572, z = 0.19860)	0.82338	0.83428	0.19860
O3	**1a** (x = -0.34296, y = 0.33906, z = 0.20332)	0.65704	0.33906	0.20332
O4	**1a** (x = 0.16402, y = 0.29482, z = 0.05794)	0.16402	0.29482	0.05794
O5	**1a** (x = 0.29345, y = -0.22926, z = 0.11592)	0.29345	0.77074	0.11592
O6	**1a** (x = 0.11225, y = -0.43309, z = 0.43249)	0.11225	0.56691	0.43249
O7	**1a** (x = 0.42931, y = 0.05512, z = 0.42114)	0.42931	0.05512	0.42114
O8	**1a** (x = -0.25066, y = -0.25500, z = -0.34748)	0.74934	0.74500	0.65252
O9	**1a** (x = -0.21913, y = 0.23955, z = -0.35672)	0.78087	0.23955	0.64328
O10	**1a** (x = 0.31633, y = 0.32431, z = -0.29168)	0.31633	0.32431	0.70832
O11	**1a** (x = 0.22936, y = -0.16496, z = -0.28848)	0.22936	0.83504	0.71152

Supplementary Table IX: Data obtained with the PBE functional ($U = 4$ eV) [2].

$BiFeO_{3-x}$ $\mathcal{M}$-FiM(Ap) [Space group $P1$]					
a (Å)	b (Å)	c (Å)	α (°)	β (°)	γ (°)
5.6800	5.6800	8.2487	91.8604	90.5656	90.0000

Atom	Wyckoff position	x	y	z
Fe1	**1a** (x = -0.02300, y = -0.48531, z = 0.20462)	0.97700	0.51469	0.20462
Fe2	**1a** (x = -0.46453, y = 0.00399, z = 0.19169)	0.53547	0.00399	0.19169
Fe3	**1a** (x = 0.01785, y = 0.49755, z = -0.32155)	0.01785	0.49755	0.67845
Fe4	**1a** (x = -0.46355, y = 0.00646, z = -0.29465)	0.53645	0.00646	0.70535
Bi1	**1a** (x = 0.02475, y = -0.04647, z = -0.03614)	0.02475	0.95353	0.96386
Bi2	**1a** (x = 0.48667, y = 0.45516, z = -0.03470)	0.48667	0.45516	0.96530
Bi3	**1a** (x = 0.04032, y = -0.05238, z = 0.48751)	0.04032	0.94762	0.48751
Bi4	**1a** (x = -0.48875, y = 0.44687, z = 0.48164)	0.51125	0.44687	0.48164
O1	**1a** (x = -0.41172, y = 0.06848, z = -0.06039)	0.58828	0.06848	0.93961
O2	**1a** (x = -0.17708, y = -0.16649, z = 0.19665)	0.82292	0.83351	0.19665
O3	**1a** (x = -0.34728, y = 0.33944, z = 0.20387)	0.65272	0.33944	0.20387
O4	**1a** (x = 0.15699, y = 0.29958, z = 0.05241)	0.15699	0.29958	0.05241
O5	**1a** (x = 0.29320, y = -0.22585, z = 0.11608)	0.29320	0.77415	0.11608
O6	**1a** (x = 0.11264, y = -0.43547, z = 0.43268)	0.11264	0.56453	0.43268
O7	**1a** (x = 0.42824, y = 0.05538, z = 0.42084)	0.42824	0.05538	0.42084
O8	**1a** (x = -0.24906, y = -0.25568, z = -0.34648)	0.75094	0.74432	0.65352
O9	**1a** (x = -0.21761, y = 0.23791, z = -0.35838)	0.78239	0.23791	0.64162
O10	**1a** (x = 0.31899, y = 0.32351, z = -0.29248)	0.31899	0.32351	0.70752
O11	**1a** (x = 0.23118, y = -0.16551, z = -0.28898)	0.23118	0.83449	0.71102

Supplementary Table X: Neutral versus charged ($q = +2\ e$) oxygen vacancies in $BiCoO_3$ thin films at $a_{in} = 3.74$ Å. From a zero-temperature energy perspective, formation of neutral vacancies is more favourable than charged vacancies, in particular, we estimate $\Delta E_{def} \equiv E_{def}[V_O^0] - E_{def}[V_O^{+2}] \sim -1$ eV (see "Methods" section in the main manuscript for the definition of E_{def} and other terms). Results are obtained with the PBE functional ($U = 6$ eV) [2] in a simulation supercell containing 4 formula units, and terms E^q_{corr} and μ_O are assumed to be identical in both the neutral and charged cases.

$E[V_O^0]$ (eV/f.u.)	$E[V_O^q]$ (eV/f.u.)	q (e)	ϵ_v (eV)	ΔV (eV)	ϵ_F^{max} (eV)	ΔE_{def} (eV/f.u.)
-26.844	-30.043	+2.0	6.650	0.998	1.110	-1.174

Supplementary Table XI: Energy difference with respect to $\mathcal{T}$-G(Ap) for several phases at different in-plane lattice parameters considering different values of U. Results are expressed in units of meV per formula unit. The PBE functional [2] was employed in these calculations.

U (eV)	2	4	6
3.78 Å			
$\mathcal{T}$-C(Eq)	-37	-2	13
3.85 Å			
$\mathcal{T}$-C(Eq)	39	70	78
3.92 Å			
$\mathcal{M}$-FiM(Eq)	16	11	-8

Supplementary Table XII: Interlayer Co-Co distances near the $\mathcal{T}$-C(Eq) $\rightarrow$ $\mathcal{T}$-G(Ap) phase transformation for different values of U (Supplementary Fig.6g). Results are expressed in units of Å. The PBE functional [2] was employed in these calculations.

	Co_1-Co_3		Co_2-Co_4	
U (eV)	2	6	2	6
3.78 Å				
$\mathcal{T}$-C(Eq)	4.66	4.64	4.66	4.64
$\mathcal{T}$-G(Ap)	4.15	4.20	4.93	4.96

Supplementary Table XIII: Magnetic moments of Co ions in the phases involved in the phase transformations $\mathcal{T}$-C(Eq) $\rightarrow$ $\mathcal{T}$-G(Ap) and $\mathcal{T}$-G(Ap) $\rightarrow$ $\mathcal{M}$-FiM(Eq) for different values of U. Results are expressed in units of μ_B. The PBE functional [2] was employed in these calculations.

	Co_1			Co_2			Co_3			Co_4		
U (eV)	2	4	6	2	4	6	2	4	6	2	4	6
3.78 Å												
$\mathcal{T}$-C(Eq)	2.5	2.6	2.7	-2.5	-2.6	-2.7	2.8	3.0	3.1	-2.8	-3.0	-3.1
$\mathcal{T}$-G(Ap)	2.5	2.7	2.8	-2.8	-3.0	-3.1	-2.4	-2.6	-2.7	2.8	3.0	3.1
3.92 Å												
$\mathcal{T}$-G(Ap)	2.5	2.7	2.8	-2.8	-3.0	-3.1	-2.4	-2.6	-2.7	2.8	3.0	3.1
$\mathcal{M}$-FiM(Eq)	2.4	2.6	2.7	-2.8	-3.0	-3.1	-2.9	-3.0	-3.2	2.4	2.6	2.7

Supplementary Table XIV: Magnetic exchange constants estimated with DFT methods (see Methods in main text and works [4–6] for technical details) for stoichiometric and non-stoichiometric BCO thin films. Results were obtained with the PBE functional ($U = 6$ eV) [2].

Phase	a_{in} (Å)	J_a (meV)	J_c (meV)	J_{ac} (meV)
$\mathcal{T}$-C	3.75	25.21	0.75	1.96
$\mathcal{T}$-C(Eq)	3.70	24.28	0.98	0.96
$\mathcal{T}$-G(Ap)	3.85	13.66	3.20	0.66
$\mathcal{M}$-G	4.00	30.56	J_a	0.00
$\mathcal{M}$-FiM(Eq)	4.00	15.87	J_a	0.00

SUPPLEMENTARY DISCUSSION

We have performed numerous comprehensive tests to assess the influence of the adopted density functional theory (DFT) exchange-correlation functional, on-site penalty energy U, size of the adopted simulation cell, concentration of oxygen vacancies, and charge of the oxygen vacancies on our theoretical conclusions. Our tests results are explained next.

Role of the DFT exchange-correlation functional

We have repeated most of the calculations presented in the main manuscript performed with the PBE exchange-correlation potential ($U = 6$ eV) [2] but employing instead the PBEsol functional [3]. Supplementary Fig.4 shows the energy, structural, and electric polarization results obtained with the PBEsol exchange-correlation potential ($U = 6$ eV) [3] in stoichiometric $BiCoO_3$ thin films. The are two major differences as compared to the PBE results reported in the main manuscript and in work [4]. First, the in-plane lattice parameters rendering the equilibrium $\mathcal{T}$, $\mathcal{O}$, and $\mathcal{M}$ structures are shifted towards lower values. For instance, with the PBE functional one obtains $a_{in}^0 = 3.76$ Å for the super-tetragonal $\mathcal{T}$ phase whereas with the PBEsol functional 3.71 Å. And second, a very small in-plane lattice parameter interval appears in which the non-polar $\mathcal{O}$ phase becomes the ground-state (we recall that when employing the PBE functional the orthorhombic phase always is metastable at zero temperature).

A very similar situation has been reported recently for bulk $BiCoO_3$ in which the $\mathcal{O}$ phase turns out to be slightly favoured over the $\mathcal{M}$ when using the PBEsol functional [6]. In that previous work, it has been concluded, based on comparisons with the experimental data available for bulk $BiCoO_3$, that the performance of the PBE functional is superior than that of PBEsol as concerns the description of phase competition and structural properties [6]. In view of such benchmark outcomes, we opted for using the PBE functional in the present work.

Supplementary Fig.5 shows the effects of considering neutral V_O's on the phase competition in $BiCoO_3$ thin films as estimated with the PBEsol DFT functional ($U = 6$ eV). In analogy to the stoichiometric case, an in-plane lattice parameter region emerges in which the $\mathcal{O}$ phase becomes the ground state, in contrast to what it is observed in the PBE case

(Fig.2 in the main manuscript). However, the general conclusions presented in the main text (namely, V_O-induced restoration of missing magnetic super-exchange interactions in large axial ratio phases and stabilization of robust ferrimagnetic states) remain invariant at the qualitative level. It is worth noting that for the series of PBE and PBEsol results the predicted lowest-energy V_O configurations and magnetic spin orderings are coincident for all $\mathcal{T}$, $\mathcal{O}$, and $\mathcal{M}$ phases (namely, $\mathcal{T}$-C(Eq), $\mathcal{T}$-G(Ap), $\mathcal{O}$-G(Ap), and $\mathcal{M}$-FiM(Eq) as one moves from compressive to moderately tensile in-plane strains).

Role of the oxygen vacancy charge

We have computed the formation energy of neutral and charged ($q = +2\ e$) V_O in $BiCoO_3$ thin films. By using the computational approach described in the "Methods" section in the main manuscript, we have estimated the quantity ΔE_{def}, defined as $E_{def}[V_O^0] - E_{def}[V_O^{+2}]$, with the PBE functional and $U = 6$ eV. Supplementary Fig.9 and Supplementary Table 10 contain the details of our ΔE_{def} calculations performed at in-plane parameters 3.78 and 3.74 Å, respectively. In both cases we find that, by neglecting the existence of likely temperature effects [7], the creation of neutral oxygen vacancies is energetically more favourable than charged V_O by about 1 eV per formula unit (in a simulation supercell containing 4 formula units). We note that in the present study we have considered all three possible phases $\mathcal{T}$, $\mathcal{O}$, and $\mathcal{M}$ when determining the lowest-energy V_O configurations (rather than just one of them [8]). Interestingly, in the charged ($q = +2\ e$) V_O case the ground state turns out be the non-polar $\mathcal{O}$-G(Ap) phase (Supplementary Fig.9c), which in the analogous neutral oxygen vacancy case does not appear to play any important role.

Role of the U on-site energy

We have explored also the effects of varying the value of the on-site penalty energy U that is employed to improve the description of transition-metal d orbitals. Supplementary Fig.6 shows the electronic-orbital occupation calculated in $BiCoO_3$ thin films with the PBE exchange-correlation potential and $U = 2$ eV; those electronic-orbital occupations have been deduced from partial electronic density plots analogous to those displayed in Figs.3 and 4 of the main text (not shown here). The are not appreciable differences with respect to

the $U = 6$ eV case. For instance, in both $U = 2$ and 6 eV cases the electrons coming out from the neutral V_O in the $\mathcal{T}$-C(Eq) phase remain delocalised over several transition-metal orbitals rather than localised in just one. Overall, the main energy competition, structural, and magnetic traits reported for $U = 6$ eV remain pretty much the same for all the phases when reasonably varying the value of U (see explanations below).

We found that the energy differences between different structures was the quantity most affected by the choice of the U parameter value. However, such a dependence of the energy differences on U does not lead to any significant variation on the conclusions presented for the two phase transformations of interest in the main text or the general phase competition diagram. This statement is supported by the numerical results reported in Supplementary Table 11. As it can observed therein, adopting smaller values of U has the principal effect of shifting the energy curves towards higher tensile strains. Meanwhile, the optimised structural parameters are barely affected by the choice of the U parameter value. This last statement is supported by Supplementary Fig.6g and Supplementary Table 12.

Regarding the estimation of Co magnetic moments, it is well-known that by increasing the value of the U parameter the hybridisation between the Co $3d$ and oxygen $2p$ electronic orbitals is reduced and consequently the computed magnetic moments of the magnetic ions turn out to be higher. Our results reported in Supplementary Table 13 are totally consistent with this expected numerical trend. It is also worth noting that the effects of the choice of the U parameter on the calculated Co magnetic moments are coherent across all the considered phases (Supplementary Table 13).

Interestingly, the results reported in Supplementary Table 13 show clearly the differences in magnetic moment between the cobalt ions that are reduced and not reduced as a consequence of the creation of oxygen vacancies (i.e., the reduced Co ions exhibit smaller magnetic moments in absolute value). It can be reasonably expected, therefore, that in the case that oxygen vacancies induced some kind of non-collinear magnetism our main conclusions on the magnetic properties of BCO thin films would remain valid. In other words, in our calculations net magnetic moments clearly are originated by uncompensated magnetic moments between species Co^{2+} and Co^{3+}, not by relative magnetic moment canting effects.

Size effects and the role of oxygen vacancy concentration

In our study, we have employed a 20-atoms simulation cell for analysing the effects of oxygen vacancies on the multifunctional properties of $BiCoO_{3-x}$ and other analogous multiferroic thin films. Such a 20-atoms simulation cell is large enough for considering all possible magnetic spin orderings and the inequivalent positions of oxygen vacancies in the relevant $\mathcal{T}$, $\mathcal{O}$, and $\mathcal{M}$ structures. Specifically, non-stoichiometric configurations have been generated by removing one oxygen atom from an apical or equatorial position in such a 20-atoms simulation cell, which renders the formula unit $BiCoO_{3-x}$ with $x = 0.25$.

The concentration of oxygen vacancies imposed in our simulations, however, may appear to be too high as compared to common experimental values of $x \sim 0.1$. Moreover, the dimensions of our simulation cell may seem a bit too small for reproducing subtle structural distortions induced by the presence of point defects. Consequently, we have carried out a number of numerical tests to evaluate the impact of size effects and V_O concentration on the predicted $\mathcal{T}$-C(Eq) $\rightarrow$ $\mathcal{T}$-G(Ap) and $\mathcal{T}$-G(Ap) $\rightarrow$ $\mathcal{M}$-FiM(Eq) phase transformations. In particular, we have performed two sets of subsidiary calculations involving (1) a 40-atoms simulation cell and two oxygen vacancies (rendering a formula unit of $BiCoO_{2.75}$) and (2) a 40-atoms simulation cell and one oxygen vacancy (rendering a formula unit of $BiCoO_{2.875}$).

Regarding the $\mathcal{T}$-C(Eq) $\rightarrow$ $\mathcal{T}$-G(Ap) phase transformation, we recall that in the simulations performed for a 20-atoms cell it was found that apical V_O induce local distortions that bring the transition metal ions situated below them closer to the remaining oxygen atoms along the out-of-plane direction. As a result, out-of-plane super-exchange interactions are partially restored and an antiferromagnetic (AFM) G state is stabilised. We have found that simulations of type (1) and (2) described above reproduce exactly this same behaviour (i.e., the explained structural distortion and consequent restoration of out-of-plane super-exchange interactions, see Supplementary Figure 10a). Thus, our conclusions obtained for the $\mathcal{T}$-C(Eq) $\rightarrow$ $\mathcal{T}$-G(Ap) phase transformation in the 20-atoms cell are robust against possible finite-size effects. It is worth mentioning that the in-plane lattice parameter at which the $\mathcal{T}$-C(Eq) $\rightarrow$ $\mathcal{T}$-G(Ap) phase transition is predicted to occur is shifted towards larger values when the concentration of oxygen vacancies is reduced. For instance, the critical a_{in} estimated for $BiCoO_{2.75}$ is 3.77 Å whereas for $BiCoO_{2.875}$ is 3.82 Å.

Regarding the $\mathcal{T}$-G(Ap) $\rightarrow$ $\mathcal{M}$-FiM(Eq) phase transformation, we also confirmed the

stabilization of a ground-state ferrimagnetic spin ordering state in the non-stoichiometric $\mathcal{M}$ phase when considering one and two oxygen vacancies in a 40-atoms simulation cell generated in different manners (Supplementary Figure 10b). In particular, for the $BiCoO_{2.875}$ composition (i.e., one oxygen vacancy in a 40-atoms simulation cell) we found that the ground-state ferrimagnetic state was 30 meV per formula unit lower in energy than the first metastable state, which was antiferromagnetic (a_{in} = 4.01 Å). Among the determined metastable phases, we observed the presence of other additional ferrimagnetic states. The total magnetization estimated for the ground-state $\mathcal{M}$-FiM(Eq) phases in our type (1) and (2) simulations described above were 0.5 and 0.25 μ_B per formula unit, respectively. The electronic mechanisms giving rise to the stabilization of the ground-state $\mathcal{M}$-FiM(Eq) phase in $BiCoO_{2.875}$ thin films are analogous to those explained in the main text for $BiCoO_{2.75}$ thin films (see Supplementary Figures 10c and 10d and Figure 4 in the main text). Therefore, our general conclusions presented for the $\mathcal{T}$-G(Ap) $\rightarrow$ $\mathcal{M}$-FiM(Eq) phase transformation in the main text are robust against possible finite-size effects.

Role of thermal excitations

In this study, thermal effects (e.g., lattice excitations) have been neglected systematically for the analysis of phase competition in non-stoichiometric $BiCoO_3$ (BCO) thin films. Such thermal excitations can be very important for determining, for instance, whether oxygen vacancy ordering (that is, when one type of V_O, either apical or equatorial, is significantly more predominant) is present or not in multiferroic oxide thin films at $T \neq 0$ conditions[7]. However, first-principles estimation of free-energies is particularly expensive, in terms of computational load, for non-stoichiometric systems owing to the low crystal symmetry and large size of the involved unit cells[4,6,7]. For this technical reason, in this study we have restricted most of our analysis to zero-temperature conditions. We note that it is certainly difficult to foresee the impact of thermal excitations on the conclusions presented in this work (e.g., is it vacancy ordering thermodinamically favourable at room temperature in BCO thin films? how do entropy effects affect the distribution of oxygen vacancies in the crystal?), and we leave further investigations on this interesting topic for future work.

Nevertheless, we have performed a simple and computationally affordable test in BCO thin films to assess the likely effects of thermal excitations on some of the main conclu-

sions presented in our study. In particular, we have calculated the vibrational Helmholtz free-energy of the $\mathcal{T}$-C(Eq) and $\mathcal{T}$-G(Ap) phases at the in-plane lattice parameter 3.78 Å, which is very close to the strain conditions at which, according to our calculations, a phase transformation between the two phases occurs at zero temperature (see Figure 2 in main text). For the calculation of vibrational Helmholtz free-energies we have considered the formula[4,6,7]:

$$F^{vib}(T) = \frac{1}{N_\Gamma}\, k_B T \sum_s \ln\left[2\sinh\left(\frac{\hbar\omega_{\Gamma s}}{2k_{\mathrm{B}}T}\right)\right] \ , \tag{1}$$

where N_Γ is the total number of wave vectors used for integration in the BZ (in the present case, we have considered only the Γ-point), ω the lattice phonon frequencies, and the summation runs over all phonon branches s.

The results of our test are shown in the Supplementary Figure 11. As it can be observed therein, the vibrational Helmholtz free-energy of the $\mathcal{T}$-G(Ap) phase is more favourable than that of the $\mathcal{T}$-C(Eq) phase at any temperature in the interval $0 \leq T \leq 400$ K, and the difference between the two quantities increases as the temperature is raised. This outcome indicates that in the $\mathcal{T}$ phase the creation of oxygen vacancies in apical positions is thermodinamically more favourable than of equatorial V_O at conditions $T \neq 0$ and $a_{\mathrm{in}} \geq 3.78$ Å. Consequently, it is very likely that our zero-temperature prediction of antiferromagnetic G-type spin ordering in super-tetragonal multiferroic thin films will be also valid for temperatures at which experiments are typically performed.

SUPPLEMENTARY REFERENCES

[1] A. V. Krukau, O. A. Vydrov, A. F. Izmaylov, G. E. Scuseria, J. Chem. Phys. **125**, 224106 (2006).

[2] J. P. Perdew, K. Burke, M. Ernzerhof, Phys. Rev. Lett. **77**, 3865 (1996).

[3] J. P. Perdew *et al.*, Phys. Rev. Lett. **100**, 136406 (2008).

[4] C. Cazorla and J. Íñiguez, Phys. Rev. B **98**, 174105 (2018).

[5] C. Cazorla and J. Íñiguez, Phys. Rev. B **88**, 214430 (2013).

[6] C. Cazorla, O. Diéguez, and J. Íñiguez, Sci. Adv. **3**, e1700288 (2017).

[7] C. Cazorla, Phys. Rev. Appl. **7**, 044025 (2017).

[8] X.-Y. Chen, L.-J. Chen, X.-B. Yang, Y.-J. Zhao, H.-C. Ding, and C.-G. Duan, J. Appl. Phys. **111**, 013901 (2012).